Speed Fluctuation Suppression Control of Super-High-Speed Electric Air Compressors Considering High-Frequency Electromagnetic Excitation

Donghai Hu, *Member, IEEE*, Jiongzhi Zhang, Jixiang Huang, Jianwei Li, *Member, IEEE*, Qingqing Yang, *Member, IEEE*, and Jing Wang

***Abstract*—With silicon carbide metal–oxide–semiconductor field-effect transistors (SiC MOSFET) being used as inverters in super-high-speed electric air compressors (SHSEAC) controllers, the high switching frequency of SiC MOSFETs would cause serious electromagnetic interference (EMI) and ulteriorly lead to speed fluctuation. Suppressing load excitation can only reduce speed fluctuations at low speeds while optimizing electromagnetic parameters can reach the same effect at high speeds. But neither of them can work at super high speed. So, this article focuses on the suppression of high-frequency electromagnetic excitation brought by SiC MOSFET through its electronic control parameters. First, we conduct dynamic modeling and analysis of SHSEAC and calculate its stability domain. Then, by designing a deep deterministic policy gradient (DDPG) speed fluctuation suppression controller, the SiC MOSFET switching frequency is controlled within the stable domain. Finally, the EMI tests were conducted on SHSEAC at rated and peak speeds. The results showed that the DDPG speed fluctuation suppression controller not only meets the CISPR 25 standard in suppressing EMI but also controls speed fluctuations below 20 r/min and reaches the production level.**

***Index Terms*—High-frequency electromagnetic excitation, SiC MOSFET, speed fluctuation, super-high-speed electric air compressor.**

I. Introduction

UNDER market demand and policy guidance, the rapid development of fuel cell heavy trucks has led to the widespread application of high-power fuel cells [1]. High-power fuel cells require a large amount of oxygen, which requires the intervention of super-high-speed electric air compressors (SHSEAC) [2], [3]. The SHSEAC's operation requires the super-high-speed permanent magnet synchronous motor (PMSM) [4], [5], [6]. SiC MOSFET can freely adjust size at super high speed, due to the high switching frequency of silicon carbide. So it is applied to the SHSEAC controller [7]. However, under the SiC MOSFET's high-speed switching, the torque's sudden change is caused by mechanical parameters, electromagnetic parameters, and electrical control parameters, which can result in speed fluctuations [8], [9], [10]. The first produces load excitation and the others produce electromagnetic excitation. The current study on suppressing speed fluctuation mainly focused on the above aspects [11].

The suppression of load excitation is mainly based on the optimization of mechanical parameters [12]. Lin and Yang [13] controlled the torque and radial force of PMSM based on sinusoidal current excitation to suppress the speed fluctuation generated by the rotor's eccentricity and imbalance. However, rotor eccentricity is only one of the changes in mechanical parameters. The study cannot solve the disturbance caused by other mechanical parameters. Cheng et al. [14] studied the mechanical parameters directly, using the Popov hyperstability theorem to estimate accurate mechanical parameters of PMSM, thereby compensating the load torque. On this basis, Liao et al. [15] identified the estimated value of mechanical parameters through the extended sliding mode observer and Luenberger observer, then adjusted control parameters in real time to suppress the fluctuation under 2000 r/min, which is in the low speed range. However, Gu et al. [16] showed that PMSM is a nonlinear system that consists of multiple variables, and the load excitation caused by mechanical parameter only has significant impact under low speeds.

The current research mainly focused on the electromagnetic parameters to suppress the fluctuation [17]. Based on the error between the reference current and the actual current in the process of PMSM's speed regulation, Zhang et al. [18] analyzed the influence caused by the current error and corrected the reference value to keep the torque stable. Hu et al. [19] studied the coupling relationship between reference voltages on the d-axis stator and q-axis stator to further propose the control method based on stability region to reduce the speed

Manuscript received 3 February 2024; revised 20 March 2024; accepted 25 April 2024. Date of publication 13 May 2024; date of current version 20 June 2024. This work was supported in part by the National Key Research and Development Program of China under Grant 2023YFE0114700 and in part by the National Natural Science Foundation of China under Grant 52377072. Recommended for publication by Associate Editor D. Xu. *(Corresponding author: Jianwei Li.)*

Donghai Hu, Jiongzhi Zhang, Jixiang Huang, and Jing Wang are with the School of Automotive and Traffic Engineering, Jiangsu University, Zhenjiang 212013, China.

Jianwei Li and Qingqing Yang are with the School of Mechanical Engineering, Beijing Institute of Technology, Beijing 100081, China (e-mail: lijianw@bit.edu.cn).

Color versions of one or more figures in this article are available at https://doi.org/10.1109/TPEL.2024.3399747.

Digital Object Identifier 10.1109/TPEL.2024.3399747

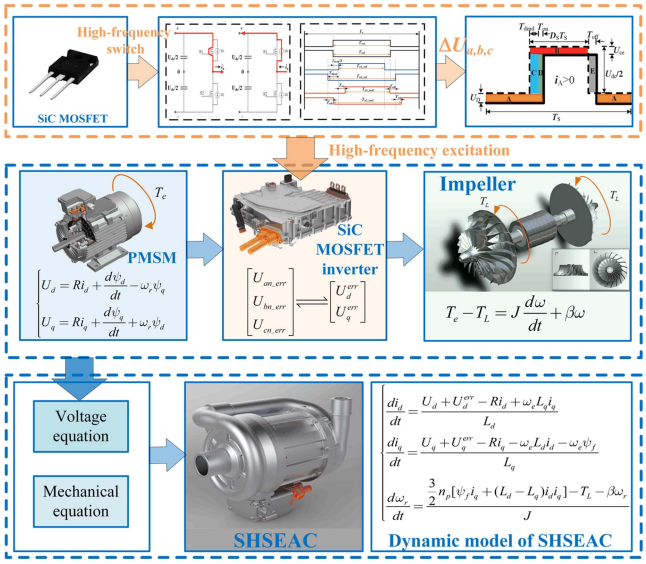

Fig. 1. Generation of high-frequency electromagnetic excitation surge.

fluctuation. But the above two studies only focused on the essential factors such as the reference current and ignored other parameters. Burye et al. [20] extracted all parameters affecting high-frequency electromagnetic excitation including shape, material, and speed through finite element analysis and applied these parameters to analytic expression. Through the analytical expression, the error of torque is calculated and compensated. However, this study still ignored some minor changes, which could have a significant impact at high speed. Aiming at the improper change moment of high-speed PMSM, Xu et al. [21] proposed a particle swarm algorithm to reduce the fluctuation in the process of flux weakening speed regulation. It could work effectively under 3000 r/min high-speed PMSM, which shows that these methods only work from low speed to high speed.

All the above references did not pay attention to the electronic control parameters in the SiC MOSFET; these could produce the distortion voltage, which ultimately triggers switching delay [22], [23], [24]. Due to the short delay time in the switching cycle, the high-speed PMSM is not sensitive to it, but the super-high-speed PMSM will produce speed fluctuation [25], [26]. To effectively control speed fluctuations within the super-high speed, this article suppresses high-frequency electromagnetic excitation through electronic control parameters. First, we construct the model of SHSEAC and calculate its stability domain. Then, the speed fluctuation is suppressed based on the deep deterministic policy gradient (DDPG) algorithm. Finally, the test bench of SHSEAC is established to verify the algorithm. The main innovations and contributions of this article are as follows.

1) Based on the physical characteristics and voltage distortion principle of SiC MOSFET, a new SHSEAC model is established which considers SiC MOSFET high-frequency electromagnetic excitation. The stable domain is calculated through this model to decide the reward function of the DDPG algorithm.
2) The speed fluctuation controller based on the DDPG algorithm was designed to solve the problem of strong coupling between the stator current on the *d-q* axis and the switching frequency, which is hard to control. The controller can continuously track the stator current on the *d-q* axis and SiC MOSFET's switching frequency to enable both of them in the stable domain.

The rest of this article is organized as follows. The establishment of the SHSEAC dynamic model and the calculation of the SHSEAC stability domain are introduced in Section II. Section III introduces the design of the reward function in the DDPG algorithm and the design process of the controller. Section IV shows the comparison of the control effect of the designed controller under training conditions and simulation conditions. In Section V, experiments are carried out on the actual super-high-speed air compressor bench to verify the effectiveness of the designed controller. Finally, Section VI concludes this article.

II. Calculation of the SHSEAC Stable Domain

A. Dynamic Model of SHSEAC

As shown in Fig. 1, the distortion problem of the output voltage of the SiC MOSFET is mainly caused by two parts: the voltage drop and the delay time [27], [28]. The voltage drop varies linearly, while the dead zone, switching delay time, and initial value of the transistor voltage drop vary nonlinearly. This leads to a certain difference between the actual voltage reference value and the ideal voltage reference value. Especially for the super-high-speed PMSM, due to the high-frequency switching of SiC MOSFET, the nonlinearity of the inverters continues to stack, and the voltage distortion effect becomes more prominent. It leads to a surge in high-frequency electromagnetic excitation. The switching frequency has a strong coupling relationship with the stator voltage on the *d*-axis (U_d) and the stator voltage on the *q*-axis (U_q), which further increases the difficulty of SHSEAC control [29], [30].

The error expression of the stator phase voltage of SHSEAC is as follows:

$$\begin{bmatrix} U_{\mathrm{an\_err}} \\ U_{\mathrm{bn\_err}} \\ U_{\mathrm{cn\_err}} \end{bmatrix} = \left[\frac{2(U_{\mathrm{dc}}-U_{ce}+U_D)(T_{\mathrm{dead}}+T_{\mathrm{ON}}-T_{\mathrm{OFF}})}{3T_s} + \frac{(U_{ce0}+U_{D0})}{6} \right] \begin{bmatrix} 2 & -1 & -1 \\ -1 & 2 & -1 \\ -1 & -1 & 2 \end{bmatrix} \begin{bmatrix} \mathrm{sgn}\,(i_a) \\ \mathrm{sgn}\,(i_b) \\ \mathrm{sgn}\,(i_c) \end{bmatrix} + \frac{(r_{ce}+r_D)}{2} \begin{bmatrix} i_a \\ i_b \\ i_c \end{bmatrix} \tag{1}$$

where U_{ce} is the voltage drop of the switching device, U_D is the voltage drop of the diode, T_{dead} is dead Time, T_{ON} is conduction delay time, T_{OFF} is turn-OFF delay time, r_{ce} is equivalent resistances of the switching device, r_D is equivalent resistances of the diode, U_{ce0} is the initial saturation pressure drop, and U_{d0} is the initial conduction voltage drop of the freewheeling diode.

According to the principle of constant amplitude, after the Clark and Park transformation of (1), the reference value of the stator voltage on the *d-q* axis and the actual value can be obtained

[31]. The error of voltage is as follows:

$$\begin{bmatrix} U_d^{\text{err}} \\ U_q^{\text{err}} \end{bmatrix} = 2\left[\frac{2(U_{\text{dc}}-U_{ce}+U_D)(T_{\text{dead}}+T_{\text{ON}}-T_{\text{OFF}})}{3T_s} + \frac{(U_{ce0}+U_{D0})}{6}\right] \begin{bmatrix} \cos\theta_e & \cos\left(\theta_e-\frac{2\pi}{3}\right) & \cos\left(\theta_e+\frac{2\pi}{3}\right) \\ -\sin\theta_e & -\sin\left(\theta_e-\frac{2\pi}{3}\right) & -\sin\left(\theta_e+\frac{2\pi}{3}\right) \end{bmatrix} \times \begin{bmatrix} \text{sgn}(i_a) \\ \text{sgn}(i_b) \\ \text{sgn}(i_c) \end{bmatrix} + \frac{(r_{ce}+r_D)}{2}\begin{bmatrix} i_d \\ i_q \end{bmatrix}. \tag{2}$$

To further simplify (2), we obtain

$$\begin{bmatrix} I_{d0} \\ I_{q0} \end{bmatrix} = \begin{bmatrix} \cos\theta_e & \cos\left(\theta_e-\frac{2\pi}{3}\right) & \cos\left(\theta_e+\frac{2\pi}{3}\right) \\ -\sin\theta_e & -\sin\left(\theta_e-\frac{2\pi}{3}\right) & -\sin\left(\theta_e+\frac{2\pi}{3}\right) \end{bmatrix} \times \begin{bmatrix} \text{sgn}(i_a) \\ \text{sgn}(i_b) \\ \text{sgn}(i_c) \end{bmatrix} \tag{3}$$

where θ is the rotor position angle, and I_{d0} and I_{q0} are the related terms of the inverter's current polarity.

Then, the error between the reference value and the actual value of the stator voltage on the d-q axis can be expressed as

$$\begin{bmatrix} U_d^{\text{err}} \\ U_q^{\text{err}} \end{bmatrix} = \left[\frac{4(U_{\text{dc}}-U_{ce}+U_D)(T_{\text{dead}}+T_{\text{ON}}-T_{\text{OFF}})}{3T_s} + \frac{(U_{ce0}+U_{D0})}{3}\right] \begin{bmatrix} I_{d0} \\ I_{q0} \end{bmatrix} + \frac{(r_{ce}+r_D)}{2}\begin{bmatrix} i_d \\ i_q \end{bmatrix}. \tag{4}$$

To combine the model of SHSEAC with the voltage model of SiC MOSFET [32], the dynamic model of SHSEAC under SiC MOSFET's high-frequency electromagnetic excitation is as follows:

$$\begin{cases} \frac{di_d}{dt} = \frac{U_d+\left[\frac{4(U_{dc}-U_{ce}+U_D)\left(T_{\text{dead}}+T_{on}-T_{off}\right)}{3T_s}+\frac{(U_{ce0}+U_{D0})}{3}\right]I_{d0}}{L_d} + \frac{\frac{1}{2}(r_{ce}+r_D)i_d - Ri_d + \omega_e L_q i_q}{L_d} \\ \frac{di_q}{dt} = \frac{U_q+\left[\frac{4(U_{dc}-U_{ce}+U_D)\left(T_{\text{dead}}+T_{on}-T_{off}\right)}{3T_s}+\frac{(U_{ce0}+U_{D0})}{3}\right]I_{q0}}{L_q} + \frac{\frac{1}{2}(r_{ce}+r_D)i_q - Ri_q - \omega_e L_d i_d - \omega_e \psi_f}{L_q} \\ \frac{d\omega_r}{dt} = \frac{\frac{3}{2}n_p[\psi_f i_q + (L_d-L_q)i_d i_q] - T_L - \beta\omega_r}{J} \end{cases}. \tag{5}$$

After the affine transformation and the timescale transformation, the above model can be converted to the following dimensionless form:

$$\begin{cases} \frac{d\tilde{i}_d}{dt} = -\tilde{i}_d + \tilde{\omega}\tilde{i}_q + \tilde{U}_d + \tilde{f}\tilde{I}_{d0} \\ \frac{d\tilde{i}_q}{dt} = -\tilde{i}_q - \tilde{\omega}\tilde{i}_d + \gamma\tilde{\omega} + \tilde{U}_q + \tilde{f}\tilde{I}_{d0} \\ \frac{d\tilde{\omega}}{dt} = \sigma(\tilde{i}_q - \tilde{\omega}) - \tilde{T}_L \end{cases}. \tag{6}$$

Among them

$$\tilde{u}_d = \frac{3n_p L_q \psi_f u_d}{2{R_1}^2\beta},$$

$$\tilde{f} = \frac{2\left(U_{dc}-U_{ce}+U_D\right)\left(T_{\text{dead}}+T_{on}-T_{off}\right)+(U_{ce0}+U_{D0})}{3T_s}$$

$$\tilde{u}_{d0} = \frac{3n_p L_q \psi_f u_{d0}}{2{R_1}^2\beta},$$

$$\gamma = \frac{n_p\psi_f^2}{R_1\beta}, \tilde{u}_q = \frac{3n_p L_q\psi_f u_q}{2R^2\beta}, \tilde{u}_{q0} = \frac{3n_p L_q\psi_f u_{q0}}{2R^2\beta}$$

$$\sigma = \frac{\beta L_q}{R_1 J}, \tilde{T}_L = \frac{L_q^2 T_L}{R_1^2 J}$$

where $\tilde{f}$ is a dimensionless parameter representing the switching frequency $1/T_s$, dead time T_{dead}, tube voltage drop $U_{ce,}$ and U_D of SiC MOSFET. Therefore, the influence of control parameters of silicon carbide MOSFET inverter on the stability of SHSEAC can be indirectly proved by studying the influence of $\tilde{f}$ on system dynamics.

B. Calculation of the SHSEAC Stable Domain

The equilibrium point of the system obtained from (6) can be expressed as

$$\begin{cases} \tilde{i}_{d0} = \tilde{\omega}_0^2 + \frac{\tilde{\omega}_0}{\sigma}\tilde{T}_L + \tilde{U}_d + \tilde{f}\tilde{I}_{d0} \\ \tilde{i}_{q0} = \frac{\tilde{T}_L}{\sigma} + \tilde{\omega}_0 \\ \tilde{\omega}_0^3 + \frac{\tilde{T}_L}{\sigma}\tilde{\omega}_0^2 + (1+\tilde{U}_d + \tilde{f}\tilde{U}_{d0} - \gamma)\tilde{\omega}_0 - \tilde{U}_q - \tilde{f}\tilde{I}_{q0} + \frac{\tilde{T}_L}{\sigma} = 0 \end{cases}. \tag{7}$$

J is the Jacobian matrix of the system at the equilibrium point, expressed as follows:

$$\mathbf{J} = \begin{bmatrix} -1 & \tilde{\omega}_{r0} & \tilde{i}_{q0} \\ -\tilde{\omega}_{r0} & -1 & \gamma - \tilde{i}_{d0} \\ 0 & \sigma & -\sigma \end{bmatrix}. \tag{8}$$

Thus, the characteristic equation of the system can be expressed as

$$\lambda^3 + A_2\lambda^2 + A_1\lambda + A_0 = 0. \tag{9}$$

It can be found that (9) is a univariate cubic polynomial equation with the coefficients as follows:

$$\begin{cases} A_2 = 2+\sigma \\ A_1 = (1+\sigma)\tilde{\omega}_{r0}^2 + \tilde{T}_L\tilde{\omega}_{r0} + 2\sigma + 1 + \sigma\tilde{U}_d + \tilde{f}\tilde{I}_{d0} - \sigma\gamma \\ A_0 = 3\sigma\tilde{\omega}_{r0}^2 + 2\tilde{T}_L\tilde{\omega}_{r0} + \sigma(1+\tilde{U}_d + \tilde{f}\tilde{I}_{d0} - \gamma) \end{cases}. \tag{10}$$

According to the Routh–Hurwitz stability criterion and bifurcation theory, the equilibrium point can be solved to produce H_{oft} bifurcation conditions:

$$\begin{cases} 2+\sigma > 0 \\ (1+\sigma)\tilde{\omega}_{r0}^2 + \tilde{T}_L\tilde{\omega}_{r0} + 2\sigma + 1 + \sigma\tilde{U}_d + \tilde{f}\tilde{I}_{d0} - \sigma\gamma > 0 \\ \left[(1+\sigma)\tilde{\omega}_{r0}^2 + \tilde{T}_L\tilde{\omega}_{r0} + 2\sigma + 1 + \sigma\tilde{U}_d + \tilde{f}\tilde{I}_{d0} - \sigma\gamma\right] \\ (2+\sigma) - [3\sigma\tilde{\omega}_{r0}^2 + 2\tilde{T}_L\tilde{\omega}_{r0} + \sigma(1+\tilde{U}_d + \tilde{f}\tilde{I}_{d0} - \gamma)] = 0 \end{cases}. \tag{11}$$

The stable domain of SHSAC and its variation law can be obtained through the Poincan bifurcation plot and the Lyapunov index [33]. In this study, the parameters of each component are shown in Table I.

To explore the stable domain variation law of dimensionless switching frequency $\tilde{f}$ under the variation of stator voltage in the dimensionless d-q axis, we assume the dimensionless q-axis stator voltage $\tilde{U}_q = 5$ and $\tilde{U}_d = -5, -10, -15, -20, -25$ and the dimensionless d-axis stator voltage $\tilde{U}_d = -15$ and $\tilde{U}_q = -5, 0, 5, 10, 15$. Draw a stable domain curve under the variation

TABLE I
MAIN PARAMETERS OF SHSEAC

parameter	numeric value	unit
Stator winding resistance, *Rm*	98	*mΩ*
d, q-axis inductance, *L*	0.25	*mH*
Rated power, *P*	28	*kW*
Viscous damping coefficient, β	0.000162	*N/(rad.s)*
Bus voltage, U_{dc}	540	*V*
Permanent magnet flux linkage, ψ_f	58	*mWb*
Air gap length, *h*	4.85	*mm*
Rated speed, n_0	90000	*.rpm*
Peak speed, n_{max}	160000	*.rpm*
Number of pole logarithms, n_p	1	
Winding method	*	

of stator voltage on the dimensionless *d-q* axis, and observe the process of stable domain variation of the dimensionless switching frequency $\tilde{f}$ of SiC MOSFET. The solid line represents the stable equilibrium point of the system, whereas the dashed line represents the unstable equilibrium point of the system. As shown in Fig. 2, when $\tilde{U}_d = -10$, the stable domains of the dimensionless switching frequency are $\tilde{f}<-110$ and $\tilde{f}>-88$. Similarly, when $\tilde{U}_q=0$, the stable domains of the dimensionless switching frequency are $\tilde{f}<25$ and $\tilde{f}>68$. When designing controllers, as the dimensionless *d*-axis stator voltage decreases, the stable region will be eroded from both sides, and the rate of decrease in the stable region in the left direction will be faster. Similarly, as the nondimensional *q*-axis stator voltage increases, the nondimensional switching frequency instability domain first rapidly expands, then gradually decreases, and overall moves to the left. It is important to avoid switching frequencies within the unstable range [34].

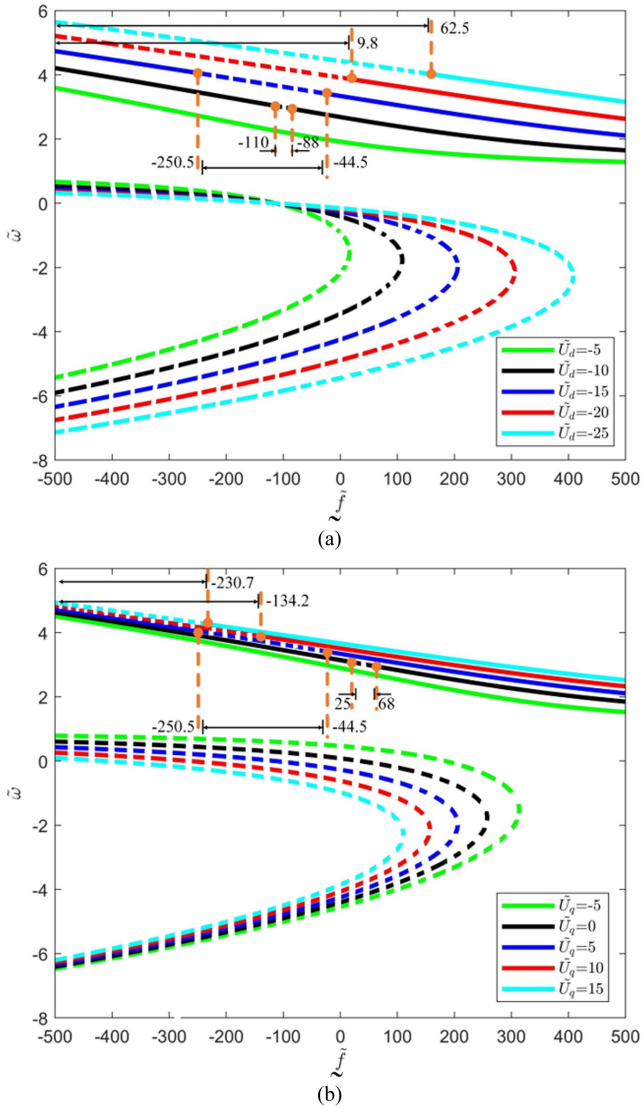

Fig. 2. Stability judgment curve of equilibrium point with (a) $\tilde{U}_d$ variation and (b) $\tilde{U}_q$ variation.

III. SUPPRESSING SPEED FLUCTUATION BASED ON DDPG

A. State and Action Setting

In the control process of SHSEAC, the state set is the state variable of the system, which can reflect the motion state of the system. In this article, the stator current tracking errors e_d and e_q of the *d-q* axis in the current loop, the PMSM speed tracking error e_ω in the speed loop, and the chaotic switching frequency error e_f are selected, as the state input of the agent action network, its vector form is expressed as follows:

$$S_t = [e_d, e_q, e_\omega, e_f]^T. \tag{12}$$

In the initial state, according to the Actor online strategy and the noise random process. The action set of the agent is the output of the Actor network, which is the vector form of optimized controller parameters U_d*, U_q*, and f_c*. It is expressed as follows:

$$a_t = [{U_d}^*, {U_q}^*, {f_c}^*]^T. \tag{13}$$

B. Design of the Reward Function

Because of the two control requirements of speed fluctuation and EMI suppression in the control of SHSEAC [33], this article sets the following reward functions.

1) Speed Fluctuation Reward Function: Steady-state error, rotational speed change rate, and other indicators should be involved in the reward function for their influence on PMSM. A comprehensive reward value can be obtained by weighting different indicators using the weight coefficients k_1 and k_2. The reward function can be expressed as

$$R_1 = r_1 - k_1\left(\frac{|\omega_t - \omega_{ref}|}{\omega_{ref}}\right)^2 - k_2\left(\frac{\omega_t - \omega_{t-1}}{\omega_{ref}}\right)^2 \tag{14}$$

where r_1 is a fixed baseline reward value, ω_t represents the current speed of PMSM, and ω_{ref} represents the desired speed value. k_1 and k_2 are the weight coefficients, respectively, that balance the effects of steady-state error and rotational speed rate

TABLE II
DDPG ALGORITHM PARAMETERS

Parameter name	numeric value
Memory pool capacity N	6000
Minimum sample set sample number n	64
The learning rate *is* η	0.002
Discount rate ξ	0.85
Weight coefficient k_1	0.0015
Weight coefficient k_2	0.0020
Weight coefficient k_3	0.0015
Weight coefficient k_4	0.0015

on the reward value. This reward function allows the controller to stabilize the speed as near as possible to the desired value and reduce the fluctuation of the speed as much as possible.

2) EMI Reward Function: Keeping the current within the desired value and minimizing current fluctuations and EMI are important. If the current on the *d-q* axis fluctuates greatly, the PMSM will produce a large EMI. So penalties should be set for current fluctuations and current errors at the same time to correct the control strategy to control the current error within a certain range. The reward function can be expressed as

$$R_2 = \begin{cases} r_2 - k_3\left(\left|i_{d(t)} - i_{d(\mathrm{ref})}\right| + \left|i_{q(t)} - i_{q(\mathrm{ref})}\right|\right) \\ -k_4\left(\left|i_{d(t)} - i_{d(t-1)}\right| + \left|i_{q(t)} - i_{q(t-1)}\right|\right) \\ \text{if } \left|i_{(t)} - i_{(\mathrm{ref})}\right| \le \mu, f \notin [f_1, f_2] \\ r_2 - k_3\left(\left|i_{d(t)} - i_{d(\mathrm{ref})}\right| + \left|i_{q(t)} - i_{q(\mathrm{ref})}\right| - \mu\right) \\ -k_4\left(\left|i_{d(t)} - i_{d(t-1)}\right| + \left|i_{q(t)} - i_{q(t-1)}\right|\right) \\ \text{else} \end{cases} \tag{15}$$

where r_2 is a fixed baseline reward value, i_{ref} is the desired current value, μ is a small tolerance value, and k_3 and k_4 are the weight coefficients, respectively, to balance the effects of stator current error and rate of change on the reward value. f_1 and f_2 are the intersections of the switching frequency stabilization domain division curve and the chaotic modulated switching frequency.

Finally, considering the speed fluctuation and EMI, the reward function is linearly integrated as follows:

$$R = R_1 + R_2. \tag{16}$$

It can be seen that k_1, k_2, k_3, and k_4 are the weight coefficients, which can be changed according to the application environment. Considering the suppression ability of speed fluctuation and EMI, the parameters are set in Table II. When R is maximum, the best optimization results will be obtained.

C. Controller Parameter Update

As shown in Fig. 3, the DDPG agent is performed by state observation, sample transfer of actions, and estimation of Q values in the Critic network. The initial value of Q will affect parameter learning. To improve the effectiveness of training, values are randomly selected from a normal distribution with a mean of 0 and a standard deviation of 0.01 to initialize the weights of the Critic network in DDPG, which is used to set the initial Q value of DDPG closer to the true Q value. Actor network

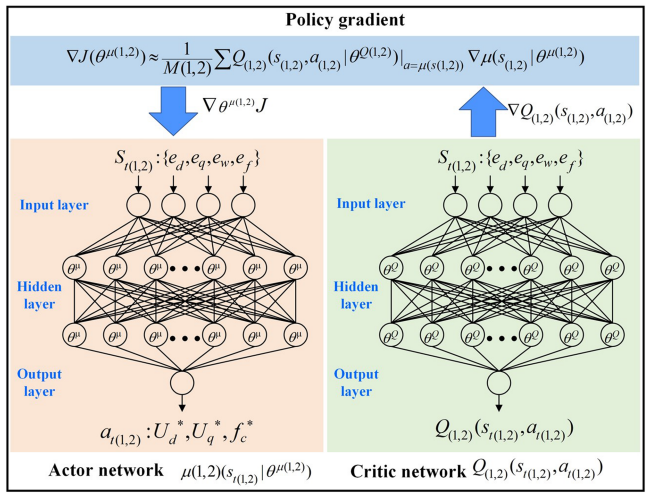

Fig. 3. Schematic diagram of parameter update for DDPG speed fluctuation suppression controller.

accepts state $s_{\mathrm{t}(1,2)}$ in the working environment of SHSEAC, outputs control action commands $a_{\mathrm{t}(1,2)}$, and the Critic network also gives a score $Q_{(1,2)}(s_{\mathrm{t}(1,2)}, a_{\mathrm{t}(1,2)})$ based on the value of the action pair in this state to help Actor network be able to output more reasonable actions in the future. The goal of the Actor network is to maximize the score of the Critic network by catering to the Critic network, so the specific parameters of the Actor network can be updated by gradient climbing given as

$$\nabla J(\theta^{\mu(1,2)}) \approx \frac{1}{M(1,2)} \sum Q_{(1,2)}(s_{(1,2)}, a_{(1,2)}|\theta^{Q(1,2)}) \Big|_{a=\mu(s(1,2))} \nabla\mu(s_{(1,2)}|\theta^{\mu(1,2)}). \tag{17}$$

The stator voltages on the *d-q* axis are $\mathrm{U}_d{}^*$ and $\mathrm{U}_q{}^*$, the estimated Q value is y_{t1}, and the chaotic switching frequency is $\mathrm{f_c}{}^*$. The estimated value y_{t2} of Q is determined by

$$\begin{cases} y_{t1} = r_{t1}\left(\{e_d, e_q, e_w\}_t, U_{d,q}{}^*\right) \\ +\gamma Q_1'\left(\{e_d, e_q, e_w\}_{t+1},\ \mu\left(\{e_d, e_q, e_w\}_{t+1}|\theta^{\mu 1}\right)|\theta^{Q1'}\right) \\ y_{t2} = r_{t2}\left(\{e_d, e_q, e_w, e_f\}_t, f_c{}^*\right) \\ +\gamma Q_2'\left(\{e_d, e_q, e_w, e_f\}_{t+1},\ \mu\left(\{e_d, e_q, e_w, e_f\}_{t+1}|\theta^{\mu 2}\right)|\theta^{Q2'}\right) \end{cases} \tag{18}$$

where $\theta^{\mu(1,2)}$ is the weight of the Actor network, $\theta^{Q(1,2)}$ is the weight of the current Critic network, and $\theta^{Q'(1,2)}$ is the weight of the target Critic network.

The Critic network weights are renewed according to the time difference algorithm to calculate the mean squared Bellman error by minimizing the loss function between the original Q value and the latest Q value, as shown in the following equation:

$$\begin{cases} L\left(\theta^{Q1}\right) = \frac{1}{M_1}\sum_t \left(y_{t1} - Q_1\left(\{e_d, e_q, e_w\}_t, U_{d,q}{}^*|\theta^{Q1}\right)\right)^2 \\ L\left(\theta^{Q2}\right) = \frac{1}{M_2}\sum_t \left(y_{t2} - Q_2\left(\{e_d, e_q, e_w, e_f\}_t, f_c{}^*|\theta^{Q2}\right)\right)^2 \end{cases} \tag{19}$$

where M (1,2) are samples of the empirical pool in the control loop, respectively.

The parameter update method of the Actor network is gradient ascent through the objective function, and the calculation formula is shown in the following equation:

$$\begin{cases} J\left(\theta^{\mu 1}\right)=\mathrm{E}\left[Q_1\left(\{e_d,e_q,e_w\}_t,U_{d,q}{}^*\right)\big|_{U_{d,q}{}^*=\mu 1\left(\{e_d,e_q,e_w\}_t\right)}\right] \\ J\left(\theta^{\mu 2}\right)=\mathrm{E}\left[Q_2\left(\{e_d,e_q,e_w,e_f\}_t,f_c{}^*\right)\big|_{f_c{}^*=\mu 2\left(\{e_d,e_q,e_w,e_f\}_t\right)}\right] \end{cases}. \tag{20}$$

The weights of the Actor network can be updated from the derivative of the objective function $J(\theta)$ via chaining rules. The Actor network is optimized by the following equation to produce the optimal control parameters of SHSEAC, as U_d*, U_q*, and $f*$:

$$\begin{cases} \nabla J\left(\theta^{\mu 1}\right)\approx\frac{1}{M_1}\sum i\left[\nabla Q_1\left(\{e_d,e_q,e_w\}_t,\right.\right. \\ \quad \left.\left.U_{d,q}{}^*|\theta^{Q1}\right)\big|_{U_{d,q}{}^*=\mu 1\left(\{e_d,e_q,e_w\}_t\right)} \\ \quad \times\nabla\mu_1\left(\{e_d,e_q,e_w\}_t|\theta^{\mu 1}\right)\Big] \\ \nabla J\left(\theta^{\mu 2}\right)\approx\frac{1}{M_2}\sum j\left[\nabla Q_2\left(\{e_d,e_q,e_w,e_f\}_t,\right.\right. \\ \quad \left.\left.f_c{}^*|\theta^{Q2}\right)\big|_{f_c{}^*=\mu 2\left(\{e_d,e_q,e_w,e_f\}_t\right)} \\ \quad \times\nabla\mu_2\left(\{e_d,e_q,e_w,e_f\}_t|\theta^{\mu 2}\right)\Big] \end{cases}. \tag{21}$$

The online actor network in the DDPG algorithm can output deterministic actions according to the state of the environment to adapt to the working environment of the electric air compressor. However, during the training process of DDPG, the updating of neural network parameters is achieved by minimizing or maximizing the objective function (Q-value). If the agent lacks exploration, the neural network parameters may fall into local optima. When there are points in the parameter space of a neural network with a gradient of zero, i.e., saddle points, the gradient descent may stop at the saddle point, leading to convergence difficulties. To improve the exploratory nature of the DDPG algorithm, reduce the risk of getting stuck in local minimum or maximum values, and enhance the algorithm's resistance to saddle points, add exploration noise ε_{12} to the Actor network, as shown in the following equation:

$$\begin{cases} U_{d,q}{}^*=\mu_1\left(\{e_d,e_q,e_w\}_t|\theta^{\mu 1}\right)+\varepsilon_1 \\ f_c{}^*=\mu_2\left(\{e_d,e_q,e_w,e_f\}_t|\theta^{\mu 2}\right)+\varepsilon_2 \end{cases}. \tag{22}$$

Both the target strategy network parameters $\theta^{\mu'}$ and the target evaluation network parameters $\theta^{Q'}$ are updated by the Soft update algorithm as

$$\begin{cases} \theta^{\mu'}=\tau\theta^{\mu}+(1-\tau)\theta^{\mu'} \\ \theta^{Q'}=\tau\theta^{Q}+(1-\tau)\theta^{Q'} \end{cases}. \tag{23}$$

The dynamic response range controlled by the speed loop and the current loop are different. The current circuit involves the electromagnetic characteristics and current response of the PMSM, while the speed circuit involves the mechanical characteristics and speed response of the PMSM. In high-speed PMSM, the response time of the mechanical system is relatively small, resulting in a relatively small impact of the speed loop on speed fluctuations. Therefore, the DDPG proxy is used to replace the current loop PI, as shown in Fig. 4. The algorithm switching frequency of DDPG is 100 Hz, the interrupt cycle is 10 ms, and the execution time of the controller is 5 ms. In the training initialization phase, the normal distribution random initialization method sets the initial value of Q in DDPG closer to

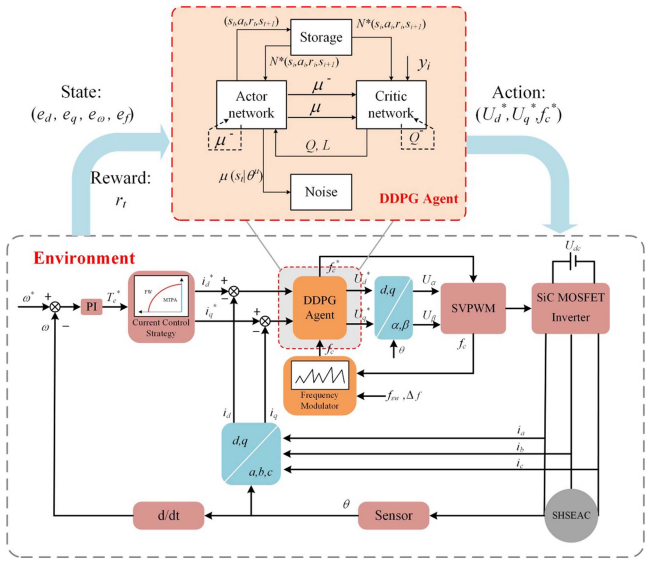

Fig. 4. DDPG speed fluctuation suppression controller block diagram.

the real value and improves the stability and convergence speed of the algorithm by adjusting the coefficients of soft updates. Effectively solves the problem in DDPG that criticizes the slow convergence of the minimum Q value of the network. Prevent the iterative output from stopping before it converges to the optimal value. In the process of algorithm training, the DDPG agent obtains the state from the working environment of the SHSEAC and then controls the action reasonably according to the state output. The environment will update the state of the next moment based on the reward feedback based on the quality of the action, and store the experience sample sequence generated by the interaction between the agent and the environment in the experience pool for parameter update optimization of the agent's own Actor-Critic network. The goal of reinforcement learning is to optimize the parameters of the agent Actor network by continuously iteratively updating the training, and finally saving the parameters in the agent Actor network after the training is completed. After that, the DDPG intelligent body can output the most reasonable control instructions in this state according to the state of the SHSEAC, to realize the suppression of the speed fluctuation of the SHSEAC.

IV. Analysis of SHSEAC Speed Fluctuation Suppression Effect

A. Comparison of Control Effects Under Simulated Conditions

The trained DDPG agent is packaged to replace the PID control module in the vector control architecture. The DDPG agent's input and output interface are redefined. Under the same parameter settings, the suppression effect of SHSEAC under different controllers is compared and simulated.

To verify the effectiveness, the target speed is set to 154 350 r/min. The simulation results of the stator voltage on the d-q axis under two different control methods are shown in Fig. 5. For the PID controller, it can be found from the simulation results

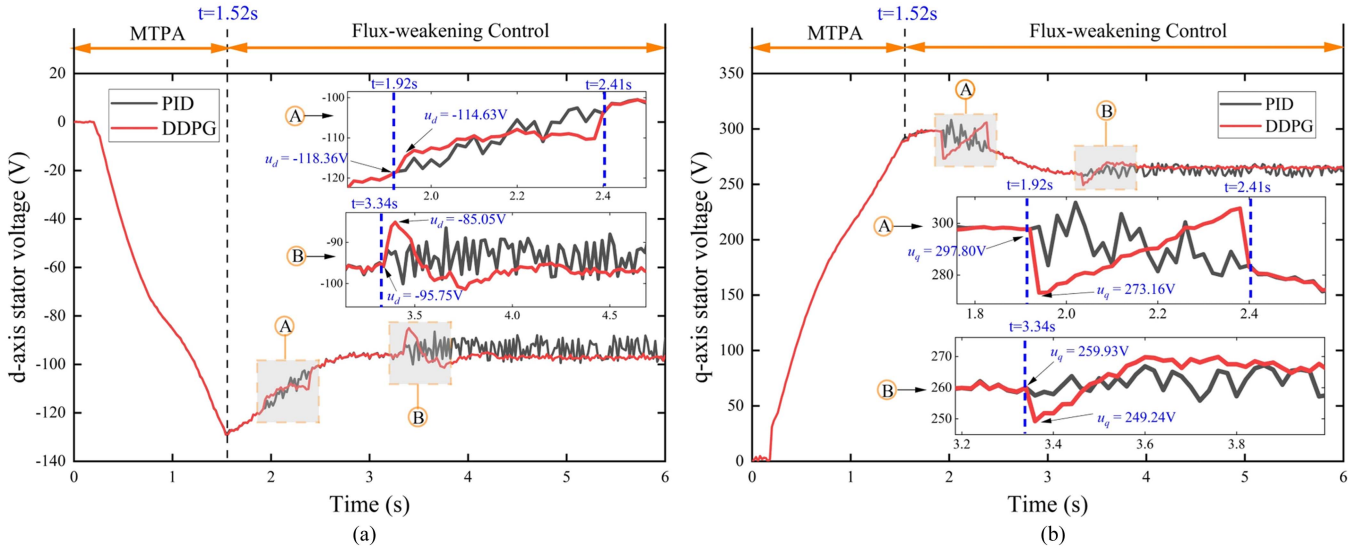

Fig. 5. Comparison of *d*-*q* axis stator voltage results between two controllers under simulation conditions. (a) *d*-axis stator voltage. (b) *q*-axis stator voltage.

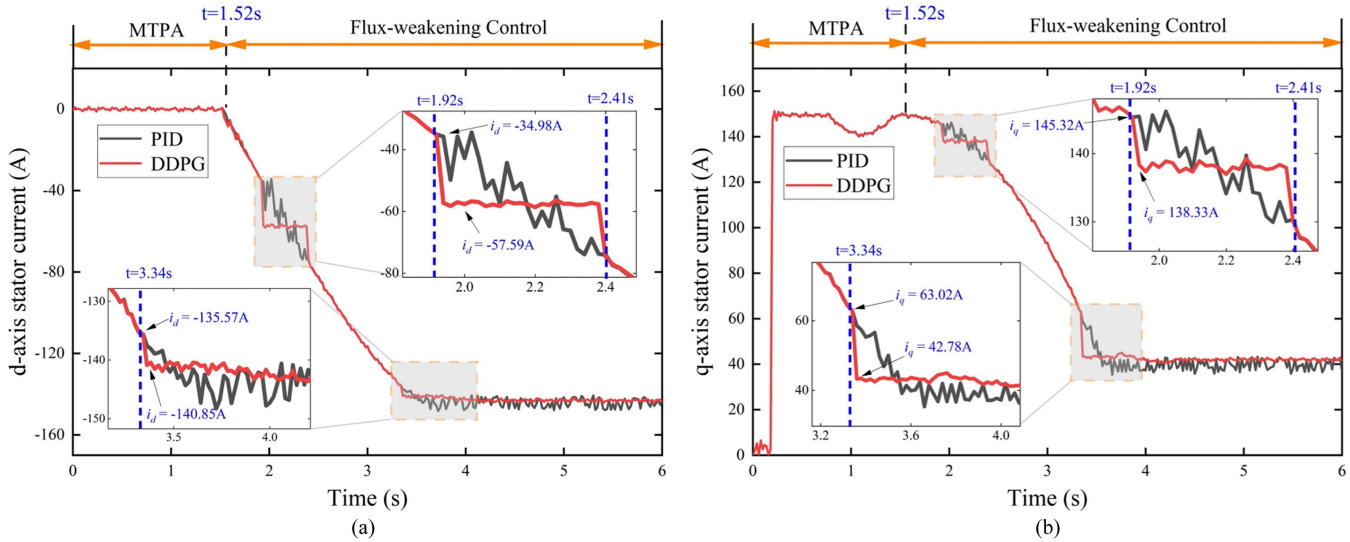

Fig. 6. Comparison of *d*-*q* axis stator current results between two controllers under simulation conditions. (a) *d*-axis stator current. (b) *q*-axis stator current.

of the stator voltage of the *d*-axis that the stator voltage on the *d*-axis begins to oscillate irregularly at $t = 1.92$ s, indicating that U_d is at this time in the unstable domain. In addition, the stator voltage on the *d*-axis continues to oscillate violently at $t = 3.34$ s, indicating that U_d has been in the unstable domain, and the PID controller is electrically charged to the stator on the *d*-axis. The pressure cannot be effectively controlled. A similar situation is also seen in the *q*-axis stator voltage simulation result plot. For the DDPG controller, it can be found from the simulation results of the stator voltage on the *d*-*q* axis that the voltage of the stator on the *d*-*q* axis is at $t =$ It was reset at 1.92 s, and the stator voltage on the *d*-axis was adjusted from −118.36 V to −114.63 V, and the stator voltage on the *q*-axis was adjusted from 297.80 to 273.16 V. From $t = 1.92$ s to $t = 2.41$ s, the DDPG controller keeps the stator voltage in the *d*-*q* axis within the stable domain. When $t = 3.34$ s, the stator voltage of the *d*-*q* axis is again set by the DDPG controller, the stator voltage of the *d*-axis is adjusted from −95.75 to −85.05 V, and the stator voltage of the *q*-axis is adjusted. The voltage is adjusted from 259.93 to 249.24 V, keeping the stator voltage in the *d*-*q* axis within the stable domain.

The simulation results of the stator current on the *d*-*q* axis under two different controllers under the simulation condition are shown in Fig. 6. For the PID controller, it can be seen from the simulation result plot that the stator current in the *d*-axis begins to oscillate irregularly at 1.92 s. In addition, the stator current of the *d*-axis oscillates continuously at 3.34 s, indicating that the PID controller cannot effectively control the stator current of the *d*-axis at this time. A similar situation is also seen in the *q*-axis stator current simulation result plot. For the use of a DDPG

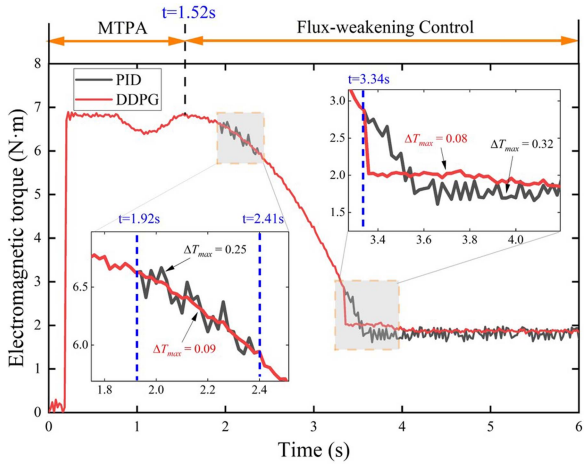

Fig. 7. Comparison of electromagnetic torque results between two controllers under simulation conditions.

controller, it can be seen from the simulation results that when the stator current on the *d*-*q* axis exists fluctuation, the DDPG algorithm sets based on the trend of current decrease. When the current reaches the expected effect, the current is stabilized by a current fluctuation penalty term. With effective stability control, the stator current on the *d*-axis is reduced from −34.98 to −57.59 A, and the stator current on the *q*-axis is reduced from 140.85 to 135.57 A. It has been stable until $t = 2.41$s. When $t =$ 3.34 s, the stator current on the *d*-*q* axis is effectively controlled by the DDPG controller again, and the stator current on the *d*-axis is reduced from −135.57 to −140.85 A. The stator current on the *q*-axis decreases from 63.02 to 42.78 A, and the stator current on the *d*-*q*-axis eventually changes smoothly following the stable current trajectory calculated by the DDPG controller.

The simulation results of the torque response under two different controllers are shown in Fig. 7. For the PID controller, it can be observed from the figure that the electromagnetic torque begins to oscillate irregularly at 1.92 s, indicating that the SHSEAC is in an unstable state, which is manifested by a large increase in speed fluctuation. In addition, the electromagnetic torque continues to oscillate violently at 3.34 s, indicating that the speed of the SHSEAC is in a continuous oscillating state at this time, and the PID controller cannot achieve stable control of the speed. For the DDPG controller, it can be seen from the figure that the electromagnetic torque is effectively controlled from 1.92 to 2.41 s. In the range, the maximum torque fluctuation amplitude is reduced from 0.25 to 0.09 N·m. In addition, at 3.34 s, the electromagnetic torque is effectively controlled by the DDPG controller again, the maximum torque ripple amplitude is reduced from 0.32 to 0.08 N·m, and the system torque fluctuation is significantly improved.

V. Experimental Verification of SHSEAC Speed Fluctuation Inhibition

A. Experimental Equipment and Methods

To verify the effectiveness of the designed DC-SVPWM modulator, it is necessary to build an SHSEAC speed response test bench, and then carry out the EMI test in the electromagnetic shielding room. As shown in Fig. 8, the SHSEAC, controller, and LISN are placed in the shielded room, as the power supply of the stabilized DC power supply and AC power supply and other auxiliary equipment are placed outside the shielded room, LISN is located in the middle of the power line, one end is connected to the output end of the power equipment, the other end is connected to the power input of the DUT. The EMI test receiver and the host computer are in a shielded room, and the data interaction and parameter setting are carried out through the test software ELEKTRA. A high-precision photoelectric encoder was mounted on the shaft of the super-high-speed electric air compressor as a sensor in this experiment to lessen the effect of speed measuring technology on the speed fluctuation of super-high-speed electric air compressors. The encoder transforms the rotor's motion into an output pulse signal. Next, the high-frequency noise in the pulse signal is eliminated and its amplitude is increased using a signal conditioning circuit that includes amplifiers and filters. Ultimately, the processed pulse signal is converted by the frequency measurement circuit into the super-high-speed electric air compressor's speed and outputted by the top computer. First, add the EMI testing receiver and LISN in the ELEKTRA testing software configuration interface to ensure normal communication between the upper computer, the EMI testing receiver, and LISN. Then, export the corresponding test equipment template in the test template library, add the correction factor of the LISN and calculate and compensate for the line loss between the EMI test receiver and the LISN wiring harness. Finally, set the relevant parameters of the conducted EMI test in the test configuration interface, the test frequency range is set to 9–30 MHz, the test mode is set to the average mode in the conducted EMI test, the test bandwidth is set to 120 kHz, and the scan rate is set to 2 kHz.

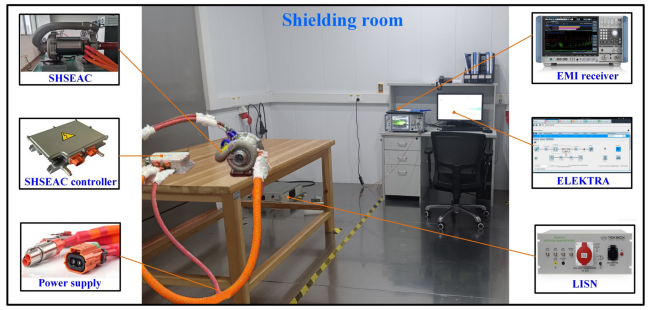

Fig. 8. EMI test bench of SHSEAC.

B. Analysis of Experimental Results

To verify the effectiveness of the designed DDPG controller, SHSEAC speed response experiments and EMI testing experiments were conducted using a dual chaotic space vector pulse width modulation (SVPWM) (DC-SVPWM) modulator for DDPG control and a DC-SVPWM modulator for the PID controller. Obtain the speed response and EMI test results under two typical operating conditions of target speeds of 97200 and 154350 r/min.

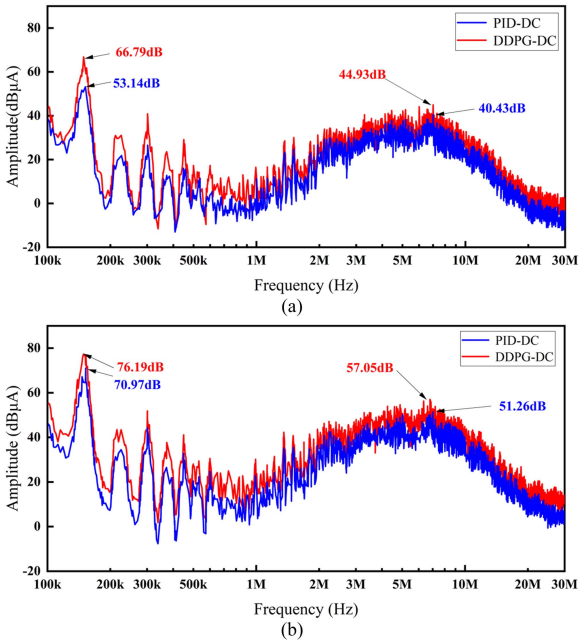

Fig. 9. Experimental results of conducted EMI testing for SHSEAC. (a) Target rotational speed of 97200 r/min. (b) Target rotational speed of 154350 r/min.

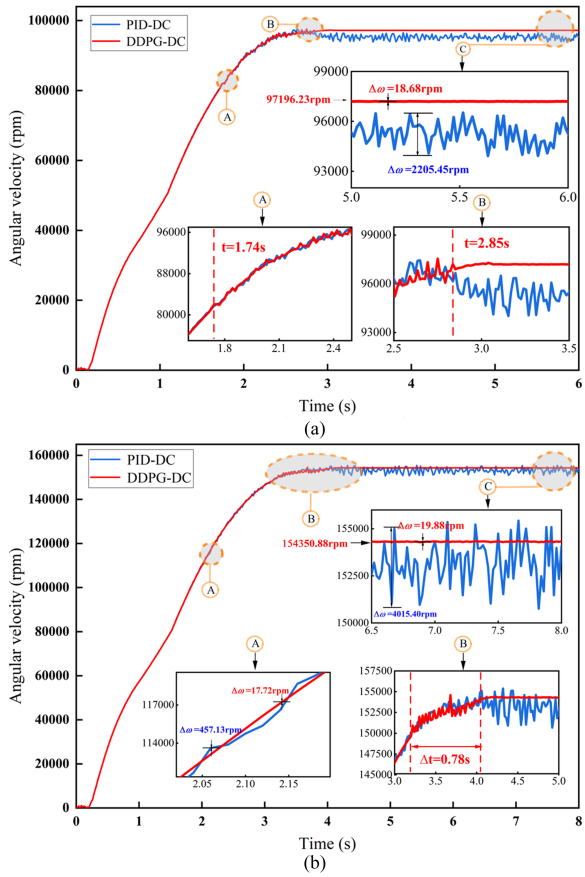

Fig. 10. Experimental results of speed response for SHSEAC. (a) Target rotational speed of 97200 r/min. (b) Target rotational speed of 154350 r/min.

The EMI curve of the air compressor target speed of 97200 r/min is shown in Fig. 9(a). In the low frequency band, the peak EMI test with PID-DC and DDPG-DC controllers: 53.14 dB and 66.79 dB, respectively. The EMI suppression effect under the PID-DC controller is 13.65 dB different from that of the DDPG-DC controller. In the high-frequency bands, the peak EMI test with PID-DC and DDPG-DC controllers is 40.43 dB and 44.93 dB, respectively. The EMI suppression effect under PID-DC control is only 4.5 dB different from that of DDPG-DC controllers.

The speed response curve of the SHSEAC with a target speed of 97200 r/min is shown in Fig. 10(a), for the speed response experiment under PID-DC and DDPG-DC two different controllers, the SHSEAC reaches the target speed around t = 2.96 s, but the steady-state performance shows obvious differences. As shown in the enlarged view of Area A in the figure, at 1.74 s, the SHSEAC gradually shows speed oscillation, and with the increase of time, the amplitude of the speed fluctuation increases rapidly, and the PMSM's control parameters are in the chaotic area. As shown in the enlarged view of Zone B and Zone C in the figure, under the PID-DC controller, the air compressor has been reaching the target speed with a fierce oscillating speed during the speed regulation, and the final speed oscillation amplitude even reaches 2205.45 r/min, at which time the air compressor is in an extremely unstable state. Under the DDPG-DC controller, the air compressor runs smoothly again at t = 2.85 s and finally reaches a speed of 97196.23 r/min. At this time, the air compressor is in a stable state, and the speed fluctuation amplitude is only 18.68 r/min, which has good steady-state performance and dynamic performance compared with the PID-DC controller.

The conduction EMI curve of the SHSEAC with a target speed of 154350 r/min is shown in Fig. 9(b). In the low bands, the peak EMI test with PID-DC and DDPG-DC controllers was 70.97 dB and 76.19 dB, respectively. Compared with DDPG-DC controller, the effect of EMI suppression under PID-DC controller is 5.22 dB different. At high frequency bands, the peak EMI test with PID-DC and DDPG-DC control devices is 57.05 dB and 51.26 dB, respectively. The effect of EMI suppression under PID-DC control is 5.79 dB different from that of the DDPG-DC controller. Under the PID-DC controller, the EMI suppression effect is good, but the corresponding speed fluctuation is obvious.

The speed response curve of the SHSEAC with a target speed of 154 350 r/min is shown in Fig. 10(b). The SHSEAC all reach the target speed around $t = 4.15$ s, but the steady-state performance shows obvious differences. As shown in the enlarged view of Area A in the figure, under the PID-DC controller, the amplitude of the speed fluctuation during the speed increase process is 457.13 r/min. With the DDPG-DC controller, the speed fluctuation is 17.72 r/min. As shown in Zone B and Zone C, under the PID-DC controller, the SHSEAC has been reaching the target speed with a fierce oscillating speed during the speed regulation process, and the final speed oscillation amplitude even reaches 4015.40 r/min, when the SHSEAC is in an extremely unstable state. Under the DDPG-DC controller, the SHSEAC

enters the unstable state again at t = 3.24 s, and after the retuning of the control parameters, the SHSEAC reenters the stable state at $t = 4.02$ s, and finally reaches 154350.88 r/min, and the speed fluctuation amplitude is 19.88 r/min, which has good steady-state performance and dynamic performance compared with the PID-DC controller.

VI. Conclusion

The main conclusions are as follows.

1) Under the peak speed condition, the EMI amplitudes of the SHSEAC under the PID-DC controller and the DDPG-DC controller are 51.26 dB and 57.05 dB, respectively, with a difference of 5.79 dB, both controllers can suppress electro-magnetic interference from SHSEAC. Among them, the EMI suppression effect of the PID-DC controller is better, but the speed fluctuation is violent, reaching 4015.40 r/min, and the serious speed fluctuation causes the SHSEAC to operate unstably.
2) After adopting the DDPG-DC controller, the SHSEAC can accurately achieve the target speed under two typical working conditions, and the speed fluctuation amplitude is always kept below the industry standard line of 20 r/min. The system has good steady-state performance and dynamic performance and also has a good performance on the EMI suppression effect, and the EMI amplitudes of the DDPG-DC controller and PID-DC controller are 44.93 dB and 40.43 dB, respectively, underrated speed conditions, the difference is only 4.5 dB.

Conflicts of Interests

The authors declare that there is no conflict of interest regarding the publication of this article.

References

[1] M. Chandran, K. Palanisamy, D. Benson, and S. Sundaram, "A review on electric and fuel cell vehicle anatomy, technology evolution and policy drivers towards EVs and FCEVs market propagation," *Chem. Rec.*, vol. 22, no. 2, 2022, Art. no. e202100235.

[2] D. Hu et al., "Waste heat utilization performance verification of heat exchanger only thermal management system for fuel cell vehicle," *J. Cleaner Prod.*, vol. 428, 2023, Art. no. 139479.

[3] D. Lu, F. Yi, D. Hu, J. Li, Q. Yang, and J. Wang, "Online optimization of energy management strategy for FCV control parameters considering dual power source lifespan decay synergy," *Appl. Energy*, vol. 348, 2023, Art. no. 121516.

[4] V. Mittal, R. Shah, N. Aragon, and N. Douglas, "A perspective on the challenges and future of hydrogen fuel," *SAE Int. J. STEEP*, vol. 3, no. 1, pp. 31–39, 2021.

[5] H. Aditiya and M. Aziz, "Prospect of hydrogen energy in Asia-Pacific: A perspective review on techno-socio-economy nexus," *Int. J. Hydrogen Energy*, vol. 46, no. 71, pp. 35027–35056, 2021.

[6] D. A. Cullen et al., "New roads and challenges for fuel cells in heavy-duty transportation," *Nature Energy*, vol. 6, no. 5, pp. 462–474, 2021.

[7] Y. Yan, Q. Li, W. Chen, W. Huang, and J. Liu, "Hierarchical management control based on equivalent fitting circle and equivalent energy consumption method for multiple fuel cells hybrid power system," *IEEE Trans. Ind. Electron.*, vol. 67, no. 4, pp. 2786–2797, Apr. 2020.

[8] H. Zhang, X. Li, X. Liu, and J. Yan, "Enhancing fuel cell durability for fuel cell plug-in hybrid electric vehicles through strategic power management," *Appl. Energy*, vol. 241, pp. 483–490, 2019.

[9] Q. Shen et al., "Design and analysis of the high-speed permanent magnet motors: A review on the state of the art," *Machines*, vol. 10, no. 7, 2022, Art. no. 549.

[10] J. H. Kim, D. M. Kim, Y. H. Jung, and M. S. Lim, "Design of ultra-high-speed motor for FCEV air compressor considering mechanical properties of rotor materials," *IEEE Trans. Energy Convers.*, vol. 36, no. 4, pp. 2850–2860, Dec. 2021.

[11] K. Kawanishi, K. Matsuo, T. Mizuno, K. Yamada, T. Okitsu, and K. Matsuse, "Development and performance of high-speed SPM synchronous machine," in *Proc. Int. Power Electron. Conf.*, 2018, pp. 169–176.

[12] Q. Zhang, H. Zhang, S. Mao, J. Li, Z. Hu, and L. Xu, "A high-speed air compressor controller for vehicle used fuel cell systems," in *Proc. IEEE Veh. Power Propulsion Conf.*, 2021, pp. 1–4.

[13] F. C. Lin and S. M. Yang, "Instantaneous shaft radial force control with sinusoidal excitations for switched reluctance motors," *IEEE Trans. Energy Convers.*, vol. 22, no. 3, pp. 629–636, Sep. 2007.

[14] L. J. Cheng, I. H. Wu, and M. C. Tsai, "Research on adaptive direct torque control based on online parameter estimation applied to surface permanent magnet motor," in *Proc. IEEE 4th Int. Future Energy Electron. Conf.*, 2019, pp. 1–7.

[15] Z. Liao et al., "An integrated observer framework based mechanical parameters identification for adaptive control of permanent magnet synchronous motor," *Complex Syst. Model. Simul.*, vol. 2, no. 4, pp. 354–367, 2022.

[16] C. Gu, X. Wang, and Z. Deng, "Evaluation of three improved space-vector-modulation strategies for the high-speed permanent magnet motor fed by a SiC/Si hybrid inverter," *IEEE Trans. Power Electron.*, vol. 36, no. 4, pp. 4399–4409, Apr. 2021.

[17] K. Ullah, J. Guzinski, and A. F. Mirza, "Critical review on robust speed control techniques for permanent magnet synchronous motor (PMSM) speed regulation," *Energies*, vol. 15, no. 3, 2022, Art. no. 1235.

[18] Y. Zhang, K. Huang, and Z. Jiang, "Speed sensorless control of PMSM based on estimated current model," *Trans. China Electrotech. Soc.*, vol. 31, no. 11, pp. 68–74, 2016.

[19] D. Hu, L. Hu, J. Wang, J. Li, and Q. Yang, "Stability enhancement optimization method for suppressing speed fluctuation under large-scale speed regulation process of super-high-speed electric air compressor," *Nonlinear Dyn.*, vol. 105, pp. 1581–1592, 2021.

[20] R. S. Burye, R. T. Arumalla, and S. Figarado, "Investigation of torque ripple in voltage source inverter driven induction motor drive operated with space vector based harmonic elimination pulse width modulation scheme," in *Proc. IEEE Int. Conf. Ind. Technol.*, 2022, pp. 1–6.

[21] W. Xu, M. M. Ismail, Y. Liu, and M. R. Islam, "Parameter optimization of adaptive flux-weakening strategy for permanent-magnet synchronous motor drives based on particle swarm algorithm," *IEEE Trans. Power Electron.*, vol. 34, no. 12, pp. 12128–12140, Dec. 2019.

[22] S. Y. Kim, W. Lee, M. S. Rho, and S. Y. Park, "Effective dead-time compensation using a simple vectorial disturbance estimator in PMSM drives," *IEEE Trans. Ind. Electron.*, vol. 57, no. 5, pp. 1609–1614, May 2010.

[23] W. Liang, J. Wang, P. C. K. Luk, W. Fang, and W. Fei, "Analytical modeling of current harmonic components in PMSM drive with voltage-source inverter by SVPWM technique," *IEEE Trans. Energy Convers.*, vol. 29, no. 3, pp. 673–680, Sep. 2014.

[24] X. Zhang, Y. Cheng, Z. Zhao, and Y. He, "Robust model predictive direct speed control for SPMSM drives based on full parameter disturbances and load observer," *IEEE Trans. Power Electron.*, vol. 35, no. 8, pp. 8361–8373, Aug. 2020.

[25] X. Ding, J. Cheng, Z. Zhao, and P. C. K. Luk, "A high-precision and high-efficiency PMSM driver based on power amplifiers and RT-SPSs," *IEEE Trans. Power Electron.*, vol. 36, no. 9, pp. 10470–10480, Sep. 2021.

[26] S. Suganthi and R. Karpagam, "Dynamic performance improvement of PMSM drive using fuzzy-based adaptive control strategy for EV applications," *J. Power Electron.*, vol. 23, no. 3, pp. 510–521, 2023.

[27] J. H. Ryu, J. H. Lee, and J. S. Lee, "Switching frequency determination of SiC-inverter for high efficiency propulsion system of railway vehicle," *Energies*, vol. 13, no. 19, 2020, Art. no. 5035.

[28] R. Zhu, T. Liang, V. Dinavahi, and G. Liang, "Wideband modeling of power SiC MOSFET module and conducted EMI prediction of MVDC railway electrification system," *IEEE Trans. Electromagn. Compat.*, vol. 62, no. 6, pp. 2621–2633, Dec. 2020.

[29] X. Zhang, J. Zhao, L. Wang, D. Hu, L. Xie, and X. Bao, "Joint Kalman observer for mechanical multi-parameter decoupling estimation of permanent magnet synchronous linear motor," in *Proc. 13th Int. Symp. Linear Drives Ind. Appl.*, 2021, pp. 1–4.

[30] J. Jiang, F. Lin, B. Li, J. Xiao, H. Zhang, and P. Ye, "A Two-step tuning method of control parameters for permanent magnet synchronous linear motor," in *Proc. IEEE 5th Adv. Inf. Technol., Electron. Autom. Control Conf.*, 2021, vol. 5, pp. 1029–1034.
[31] C. Wang, J. Pan, Y. Hong, and Y. Liu, "Design mechanism of sampling frequency on mechanical parameter identification in a two-mass servo drive system," in *Proc. 22nd Int. Conf. Elect. Mach. Syst.*, 2019, pp. 1–5.
[32] C. Wang, L. Xin, and J. Pan, "Identification of mechanical structure for servo drive system," in *Proc. 8th Int. Conf. Power Electron. Syst. Appl.*, 2020, pp. 1–4.
[33] I. López, E. Ibarra, A. Matallana, J. Andreu, and I. Kortabarria, "Next generation electric drives for HEV/EV propulsion systems: Technology, trends and challenges," *Renewable Sustain. Energy Rev.*, vol. 114, 2019, Art. no. 109336.
[34] D. Hu, Y. Yan, and Z. Li, "Optimization methodology for control parameter of PI based on chaos prediction of electric powertrain," *AIP Adv.*, vol. 8, no. 9, 2018, Art. no. 095115.

Donghai Hu (Member, IEEE) received the B.S. degree in vehicle engineering and the Ph.D. degree in automobile engineering from Jiangsu University, Zhenjiang, China, in 2011 and 2016, respectively.

He is currently an Associate Professor with the School of Automotive and Traffic Engineering, Jiangsu University. His research interests include waste heat utilization and temperature control of fuel cell vehicles, energy management strategy of new energy vehicles, and hydrogen energy and safety.

Jiongzhi Zhang received the B.S. degree in automation from Shaoguan University, Guangdong, China, in 2014, and the M.S. degree in vehicle engineering from Jiangsu University, Zhenjiang, China, in 2023.

His current research focuses on nonlinear dynamics.

Jixiang Huang received the B.S. degree in vehicle engineering from the School of Automotive Engineering, Changan University, Xi'an, China, in 2021, and the M.S. degree in vehicle engineering from Jiangsu University, Zhenjiang, China, in 2024.

His research interests include energy management of fuel cell vehicles.

Jianwei Li (Member, IEEE) received the B.Eng. degree from North China Electric Power University, Beijing, China, in 2012, and the Ph.D. degree from the University of Bath, Bath, U.K., in 2017, both in electrical engineering.

He was with the University of Liege, the Beijing Institute of Technology, and the University of Oxford. His research interests include electrical energy storages and hybrid energy storages, electrical vehicles, batteries, fuel cells, power management of multivector systems, and hydrogen energy and safety.

Qingqing Yang (Member, IEEE) received the Ph.D. degree in electrical engineering from the University of Bath, Bath, U.K.

She was a Lead Engineer in electrical engineering with the Beijing Electric Power Research Institute, State Grid Corporation of China. She was a Lecture with Coventry University. She is currently a Professor with the School of Mechanical Engineering, Beijing Institute of Technology, Beijing, China. Her research interests include HVdc control and protection, applied superconductivity, virtual inertia in power systems, and artificial intelligence applications in energy storage and smart grids.

Jing Wang received the B.S. degree in mechanical engineering from the Yancheng Institute of Technology, Yancheng, China, in 2011, and the M.S. degree in vehicle engineering from Jiangsu University, Zhenjiang, China, in 2014.

Her research interests include fuel cell systems and the design and simulation of cooling systems.